13

Heliophysics with radio scintillation and occultation

MARIO M. BISI

There are multiple techniques that can be employed to study the Sun and solar wind. Remote-sensing observations include radio and visible/white-light observations of the Sun from the ground, and observations in the ultraviolet (UV) and X-ray bands from space along with any other parts of the electromagnetic (EM) spectrum. The density irregularities in the solar wind can also be observed using ground-based or space-based coronagraphs for the inner solar wind as it emerges from the Sun's corona, by space-based white-light heliospheric imagers, and by radio measurements of distant compact radio sources to indirectly observe the solar wind through scintillation in the radio signal received from distant astronomical or artificial radio sources.

In-situ measurements of solar-wind velocity, density, magnetic field, temperature, and other plasma and field parameters are also of high importance. An advantage of in-situ measurements is that the physical parameters recorded are measurements of the primary solar wind parameters at that point in space and time. However, the obvious disadvantage to this is that measurements can be made only at that particular position of the spacecraft at certain times. Some regions are only accessed rarely, if ever; for example, in-situ measurements inside of 0.3 AU (the perihelion of the orbit of the planet Mercury) or outside of the ecliptic plane of the solar system are not available at present. Only the Ulysses spacecraft data set is available for past years outside of the ecliptic (1990 launch, mission data from 1994 to 2009) and some measurements are available from the twin Helios spacecraft both outside of the ecliptic and just inside the orbit of Mercury (1974 and 1976 launches, mission data from 1975 to 1985). Remote-sensing observations have the advantage of covering the solar wind over a wide range of heliocentric distances and all heliographic latitudes (including out of the ecliptic plane) and at almost any time; this is especially true of radio observations. The disadvantage to remote-sensing observations is that the primary parameters are not measured but are inferred from the observations.

13.1 Observing radio waves

The radio spectrum itself is broken down into various segments as defined through radio astronomy (see Table 13.1). It is important to remember that frequencies below about 10 MHz (sometimes as high as below 30 MHz, depending on ionospheric conditions) can only be observed outside of the Earth's ionosphere because these lower radio frequencies are reflected by the ionosphere and hence cannot propagate through from space to the ground.

13.1.1 The Sun and radio waves

James Clerk Maxwell (1831–1879) was the first to theoretically predict the existence of EM waves by the derivation of his equations that describe mathematically how electric induction occurs from an oscillating magnetic field and showed that they traveled at the speed of light and that light, too, was just another form of EM radiation (Maxwell, 1873). The original paper on the theory behind his equations was read before the Royal Society on 8 December 1864. Heinrich Hertz (1847–1894) confirmed during the years 1885–1889 that radio waves existed and was the first to send and receive them. In 1901, Gugliemo Marconi (1874–1937) was the first to send a radio message across the Atlantic Ocean from England to Canada using the Earth's ionosphere to reflect the radio waves (although the nature of this reflectivity was not known at the time).

The "great storms" of radio emission from the Sun in February of 1942 were the beginning of the modern development of radio astronomy. The 1942 detection occurred when British military radar stations that were operating at wavelengths of the order of a few meters experienced some form of jamming in late February of that year. An investigation described by Hey (1983) led to the conclusion that radio waves of very high intensity were being emitted from the Sun and were apparently due to a very large presence of sunspots that were active on the solar disk. Later that same year, Southworth (in the USA) discovered that the quiet Sun also emitted solar radio waves; this was the normal radio emission from the Sun at centimeter wavelengths (Hey, 1983).

In 1951, when observations of the outer solar corona were underway, it was noticed that radio waves were coming from the Crab Nebula. These radio waves were refracted due to the electron-density irregularities in the solar corona which caused the apparent size of the Crab Nebula to increase as observations of the radio waves moved in closer to the Sun where the Crab Nebula was going behind the Sun on the sky (Hewish, 1955). Interplanetary scintillation (IPS) of the radio waves from distant compact radio sources produced by density variations in the

Table 13.1 *A breakdown of the radio spectrum. N.B. Frequencies below about 10 MHz and sometimes as high as below 30 MHz can only be observed outside of the Earth's ionosphere.*

Frequency band definition	Frequency range	Wavelength range	Band designations
ELF – Extremely Low Frequency	<300 Hz	>1000 km	—
ULF – Ultra Low Frequency	300 Hz–3 kHz	1000 km–100 km	—
VLF – Very Low Frequency	3 kHz–30 kHz	100 km–10 km	—
LF – Low Frequency	30 kHz–300 kHz	10 km–1 km	—
MF – Medium Frequency	300 kHz–3 MHz	1 km–100 m	—
HF – High Frequency	3 MHz–30 MHz	100 m–10 m	—
VHF – Very High Frequency	30 MHz–300 MHz	10 m–1 m	—
UHF – Ultra High Frequency	300 MHz–3 GHz	1 m–100 mm	P (sometimes) = 300 MHz–1 GHz L = 1 GHz–2 GHz S = 2 GHz–4 GHz C = 4 GHz–8 GHz
SHF – Super High Frequency	3 GHz–30 GHz	100 mm–10 mm	X = 8 GHz–12 GHz Ku = 12 GHz–18 GHz K = 18 GHz–26 GHz Ka = 26 GHz–40 GHz Q = 30 GHz–50 GHz U = 40 GHz–60 GHz V = 50 GHz–75 GHz
EHF – Extremely High Frequency	30 GHz–300 GHz	10 mm–1 mm	E = 60 GHz–90 GHz W = 75 GHz–110 GHz F = 90 GHz–140 GHz D = 110 GHz–170 GHz

solar wind further out from the Sun were discovered soon afterwards (Hewish *et al.*, 1964; Cohen *et al.*, 1967) and have now been in almost constant use in an effort to determine some of the properties of the solar wind via radio remote sensing.

In all, there are four primary methods of observing the Sun by radio waves: radio emissions both from the Sun itself and from the solar wind (such as from the electron beams responsible for solar radio bursts, as well as both coherent and incoherent emission); radar echoes where radio waves sent to the Sun reflect off the solar atmosphere; the Faraday rotation of polarized spacecraft beacons or astronomical radio sources (such as by pulsars or the background galactic synchrotron radio emission) due to changes in the magnetic field in the solar corona (and the solar wind); and IPS with compact astronomical radio sources (such as quasars, or occasionally with spacecraft beacons). A broader introduction to the radio aspects of the Sun and inner heliosphere not covered in this chapter can be found in Ch. 4 of Vol. II.

13.2 Astronomical radio sources and spacecraft beacons

Quasars, otherwise known as quasi-stellar radio sources, are most typically used for observations of IPS. They are compact, broadband radio emitters. Quasars are extremely luminous and the most-energetic and distant type of phenomena classified as Active Galactic Nuclei (AGN). AGN quasars can be 100 times more luminous in radio light than the whole Milky Way galaxy, and are extremely compact on the sky plane.

Fast-rotating neutron stars that make pulsars are created as a result of Type II supernovae of stars between about eight and 25 solar masses. These too are compact, broadband radio emitters on the sky. They are very small objects being some tens of kilometers in diameter between about 1.5 and five solar masses that rotate very fast. The pulse comes from a beam of high-intensity radiation being emitted from the pulsar's magnetic axis which spins with the neutron star where the magnetic axis determines the direction of the electron beam, but is not necessarily aligned with the rotational axis of the neutron star; hence the pulsing observations as viewed from the Earth.

Spacecraft radio beacons emit radio waves at one or more known frequencies that for use in heliophysics are usually in the S or X band of the radio spectrum (but also at much lower frequencies depending on the spacecraft beacon design specifications). They are normally wholly circularly polarized in either a left-handed or right-handed sense, but will have a small polarization leakage into the other polarization. They are typically used to track the spacecraft position, but can be used to obtain properties of the solar corona, solar wind in the heliosphere, and even of planetary atmospheric properties.

13.3 Radio occultation

An occultation occurs when one object is hidden by another that passes between it and the observer; i.e., when an apparently larger body passes in front of an apparently smaller one. Radio occultation is another remote-sensing technique, but is generally used for determining the physical parameters of planetary atmospheres, although a similar technique can be used for observations of spacecraft beacons as spacecraft move behind the Sun. It is the result of refraction of a radio wave by a planetary or the solar atmosphere.

For planetary occultation, the bending of the radio waves is a result of the different properties in the planetary atmosphere/ionosphere, and thus the amount of bending is determined by these properties. At radio frequencies the amount of bending cannot be measured directly but can be calculated using the Doppler shift of the signal given the geometry of the radio emitter and the radio receiver. In the case of neutral atmosphere properties, those below the ionosphere in particular, properties such as the water vapor content, atmospheric pressure, and the gas temperature can be derived, so that radio occultation has some direct applications for the meteorology aspects of heliophysics.

13.4 Radio scintillation

The term scintillation, known more commonly as twinkling, is the generic term for variations in apparent brightness or position of a distant luminous object viewed through some medium. There are several types of radio scintillation that can occur, each with different causes, and each somewhat dependent on the source size on the sky, on where from the Earth it is observed, and also on the frequency that it is observed at.

For the most extended astronomical radio sources (as well as for spacecraft and satellite communications/beacons in general) the only real contributor for scintillation is that of the Earth's ionosphere. Ionospheric scintillation is caused by turbulent structures in the ionosphere that scatter the incoming radio waves forming an interference diffraction pattern by varying the path length along which the waves reach a telescope. Ionospheric scintillation can cause the biggest concern for global navigation systems, for example, because the scintillation can cause an error in the timing from the satellite and hence can give an inaccurate position measurement. Ionospheric scintillation is generally predominant at lower radio frequencies and also at high Earth magnetic latitudes, but during high solar activity and resulting space weather at the Earth the effects can also be seen at much lower latitudes (and even at the higher observing frequencies). Thus, ionospheric scintillation can also cause problems for radio astronomy and can sometimes dominate over other aspects of a radio signal and over other types of scintillation that are of scientific interest.

If you were to use "point-like" compact astronomical radio sources, then for milli-arcsecond source sizes on the sky, you can also get IPS in your radio signal under the right conditions. This form of scintillation is a result of density inhomogeneities and turbulence in the solar-wind plasma outflow from the Sun. This also results in the scattering of the radio waves, but for a sensible scintillation pattern to be formed which can then be used for the study of the solar-wind plasma, the source ideally needs to be simple and not complex in nature. This means that the radio emission needs to be coming from a single point. The sources are usually within 90° elongation from the Sun (although IPS can occur for signals received from radio sources beyond 90° elongation, i.e., radio sources on the sky in the anti-solar direction). In addition, throughout the late 1960s, IPS was also used extensively for the study of the source structure of quasars before the advent of very-long-baseline interferometry (VLBI), which combines multiple telescopes together to form a single, much-larger overall collecting area, and much-enhanced imaging resolution.

In an even-more "point-like" compact sense, micro-arcsecond source sizes on the sky can be used for interstellar scintillation or ISS (for example, a 10 μarcsec source size in radio would be about 10 000 times finer in terms of the resolution needed than is achieved by the Hubble Space Telescope operating at its shortest wavelength). ISS can provide information on the speed and direction of flows in the interstellar medium (ISM), just as IPS does for the interplanetary medium, but only if the radio source is that much more compact.

13.5 Radio occultation, with a focus on planetary occultations

Planetary occultation is detected through the effects on the radio-wave propagation resulting in changes in the velocity of the radio waves from that in free space. In addition, changes in the frequency, phase, and amplitude of the signal, and also changes in the refractive index and hence the amount of bending of the radio waves caused as a result of the planet occulting the spacecraft. Similar effects are also observed with solar occultations, but for different parameters and methods, one of which being the detection of Faraday rotation (FR) which is covered in Sect. 13.7 as well as for higher-frequency observations of IPS as covered by Sect. 13.6.

The technique of planetary occultation has been proven to be important for the study of planetary atmospheres (e.g., Eshleman, 1973). However, as with all observing techniques, there are uncertainties involved with the experiment, and these are well documented in the literature (e.g., Withers, 2010).

The effects of planetary occultation on radio signals come from many aspects of a planetary atmospheric–ionospheric environment. Thus, radio occultations probe

both lower atmospheric properties (neutrals/molecules) as well as ionospheric electron densities.

The first use of a coherent radio transmission for investigating planetary atmospheres/ionospheres other than that of the Earth was on 15 July 1965 with the Mariner IV spacecraft as it disappeared behind the limb of Mars. The spacecraft remained in occultation for around 54 min and, prior to the start and immediately following the occulation, the spacecraft's S-band radio signal passed through both the atmosphere and the ionosphere of Mars. This first is well documented by Kliore *et al.* (1965) where Doppler tracking was also used for this experiment. Planetary occultation relies on the interaction of the radio signal being transmitted with the planetary atmosphere for any effects in the radio-wave propagation to be recorded and for the experiment to work (e.g., Withers, 2010).

Details on the atmosphere of Venus have been discovered through several occulation experiments from multiple spacecraft whereby the temperatures, densities, and cloud layers have been determined and investigated with height above the planet's surface (e.g., Imamura *et al.*, 2011, and references therein). Figure 2 of Imamura *et al.* (2011) provides an excellent image example of how the radio signal is refracted due to a planet's atmosphere/ionosphere, along with a full description and set of equations explaining such.

A list of key references of giant-planet occultation observations is given in Table 8.1, along with an extensive list of the basic planetary and upper-atmospheric properties that can be gleaned from the use of radio-occultation measurements due to planetary atmospheres. In addition, Fig. 8.4 provides examples of ionospheric electron-density profiles as derived from spacecraft radio occultation experiments carried out at Jupiter, Saturn, Uranus, and Neptune, and their respective altitudes refer to the radial distance above the one bar pressure level of atmosphere. Despite these experiments, any detailed knowledge of ionospheric structure at the giant planets is still relatively unconstrained by observation. This is because the radio-occultation experiments at these planets remain to be few with only nine published experiments for Jupiter, 31 for Saturn, two for Uranus, and two for Neptune. So even less is known about the ice giants than the gas giants.

Saturn has had the greatest amount of scientific investigation carried out via radio-occulation measurements, and this is mostly due to the Cassini spacecraft being in orbit there since 1 July 2004. This far-increased number of radio-occultation measurements has allowed for the identification of two main global ionospheric structures. These are in the form of dawn/dusk asymmetries and an unexpected behavior in how the electron density varies with changing latitude in that the electron densities are actually smallest at the equator. Further details of these findings can be found in Ch. 8, and also in Nagy *et al.* (2006, 2009), and Kliore *et al.* (2009).

Coming back to Mars, dust storms provide an episodic forcing on the upper atmosphere and ionosphere of Mars where, thus far, there has not been found an analog at Earth and thus this is of high interest since it is something not able to be investigated at Earth. The dust storms can be regional or global in nature, and are also very much unpredictable in their occurrence and ferocity. There appears to be a time where dust storms are more prevalent on Mars, and this has been termed the "dust storm season", and it encompasses the second half of the year on Mars (Zurek *et al.*, 1992; Kass *et al.*, 2014). Dust storms have the effect of changing the normal radio-occulation recording parameters for experiments conducted through Mars' upper atmosphere, and further details of these can be found in Ch. 9. As an example, Fig. 9.15 clearly illustrates that for an event which took place in 2005 on Mars, the dayside heights of the atmosphere rose by 5 km as a result of the dust storm taking place. This and other effects have been measured through the radio-occulation technique. Profiles for the Mars atmospheric environment can also be found in, e.g., Tellmann *et al.* (2013), and references therein, as well as the detection of gravity waves, which is of a high importance since it is thought that gravity waves have a significant influence on the atmospheres of the other terrestrial planets, including the Earth (e.g., Tellmann *et al.*, 2013).

A detailed discussion of the Earth's ionosphere, where planetary occultation methods are still used, as well as space-weather effects on and as a result of the ionosphere, are well documented and described in the chapter by Norbert Jakowski in Vol. V (cf., Table 1.2). In addition, the latest advances in ionospheric scintillation where the secondary power spectrum of an observation can provide a distance to the scattering screen responsible for the scintillation (see Sect. 13.6 for the description in relation to IPS), i.e., the height of the ionosphere's scattering screen are given in Fallows *et al.* (2014).

13.6 Interplanetary scintillation in the context of heliophysics

13.6.1 A brief history of IPS and IPS-capable receivers

In 1951, Vitevitch in Russia, and both Machin and Smith at Cambridge, independently suggested the possibility of studying the outer solar corona by using observations of distant radio sources. This arose from observations of the radio component of the Crab Nebula whereby its apparent size seemed to change and broaden as a result of the scattering of the radio waves by variations/inhomogeneities in the coronal electron density (described in Hewish, 1955; Brandt, 1970; and Hey, 1983). An extension of this was that of interplanetary scintillation; this technique was developed by Hewish from 1962 onwards (Hewish *et al.*, 1964) following the serendipitous discovery of unusual fluctuations in source signal strength during a program to accurately map the position of a large number of radio sources on the

sky. These astronomical radio sources were subsequently determined to be "point like" in nature (P. J. S. Williams, private communication to A. R. Breen, 2002, as cited in Canals, 2002; Bisi, 2006). It was thus hypothesized that these same density irregularities causing the broadening of the Crab Nebula radio-source size were also responsible for the scintillation in the radio waves from the distant point-like sources, and also that the solar corona extended out into the interplanetary medium (subsequently coined as the solar wind). It was then recognized that IPS could be a powerful tool in probing the solar wind and also for measuring the finer structure of the radio sources themselves (Hewish *et al.*, 1964; Hewish and Okoye, 1965).

The amount of scintillation detected at Earth was suggested to be highly dependent on the elongation angle of the source from the Sun (i.e., the distance from the point of closest approach, the P-point, of the Earth-to-source line of sight (LOS) to the Sun), and that, beyond some critical elongation angle, the scintillation would no longer be detectable by the receiver. This critical elongation angle was described as "the effective radius of the corona for occultation", which was proposed to be dependent on the effective wavelength being observed (for more details, see Machin and Smith, 1952). Hence, the possibility was then suggested that you could estimate the electron density of the corona by measuring the occultation radius over a range of different wavelengths.

Hewish's first observations of IPS gave solar wind velocity estimates of between $200\,\mathrm{km\,s^{-1}}$ and $400\,\mathrm{km\,s^{-1}}$. It was IPS that first indicated that the velocity of solar wind was greater coming from above the polar regions of the Sun than was observed in the plane of the ecliptic (Dennison and Hewish, 1967; Coles *et al.*, 1980). This was due to IPS being capable of observing at all heliographic latitudes wherever there are suitable radio sources on the sky. This discovering of faster wind over the Sun's polar regions was then only later confirmed by the Ulysses polar pass in-situ measurements many years later (Phillips *et al.*, 1994). Similarly, Houminer (1971) found features in IPS that are transient and those that co-rotate.

Multi-site observations of IPS were subsequently extensively undertaken from the early 1970s onwards via the use of several different systems around the world over the years. For example, up until 1987, scientists at the University of California, San Diego (UCSD) described in a series of papers (Armstrong and Coles, 1972; Armstrong *et al.*, 1972; Coles and Rickett, 1976; Coles *et al.*, 1980; Rickett and Coles, 1991; Rickett, 1992) observations that were undertaken at a frequency of 74 MHz with a maximum baseline of 94 km using a three-antenna system. These observations of IPS provided results that gave an overview of changes in the solar wind over a whole solar cycle covering all heliographic latitudes. These results showed a large change in the nature of the solar-wind structure throughout the solar cycle and also followed the magnetic evolution of the inner corona (Rickett and Coles, 1991). The declining phase of that cycle, which lasted for seven years,

saw the high-latitude heliosphere dominated by near-uniform fast flow occupying approximately half of the heliosphere in all. This was the same during the solar minimum itself. The low helio-latitudes were dominated by a low-velocity flow from around the heliospheric current sheet. A latitudinal gradient could be seen at solar minimum which then vanished at solar maximum, with slow flow extending to all latitudes during the period of, and around, the maximum activity (Coles and Rickett, 1976; Coles *et al.*, 1980). In addition, over in Japan (and covering the same time period), observations of IPS were conducted by scientists at the Solar Terrestrial Environment Laboratory (STEL/STELab) at Nagoya University (Kojima and Kakinuma, 1987), now the Institute for Space-Earth Environment (ISEE). These observations continue even today at a higher frequency of 327 MHz, and thus were used and are being used to probe closer to the Sun than the UCSD system (the reasons for this are discussed later in this chapter). Observations of IPS at a higher frequency of 933.5 MHz began in 1982 at the European Incoherent SCATter (EISCAT) radar facility based across northern Scandinavia (Bourgois *et al.*, 1985) which allowed for the determination of solar wind parameters from around 20 $R_\odot$ to over 75 $R_\odot$; these were the closest-in multi-site observations of IPS at the time.

The resolving ability of such multi-site observations of IPS was also improved using EISCAT due to the much larger baselines of up to 390 km. These observations were able to show simultaneously from individual observations that there were two clear solar wind components ahead of any confirmation by the Ulysses spacecraft. EISCAT (Rishbeth and Williams, 1985) has been used for IPS-observing campaigns regularly since 1985 and more extensively from 1991. A unique opportunity arose in 1994 and 1995 for a comparison with the in-situ measurements from 1.4 AU and outward of the Ulysses spacecraft as it passed over the poles of the Sun reaching latitudinal extents of 80.2° South and North. This bi-modal nature of the solar wind was determined with the fast stream of around 800 km s^{-1} and slow stream around 400 km s^{-1} (Breen *et al.* 1996a, b). These then agreed with data taken using the Ulysses spacecraft (Phillips *et al.*, 1994, 1995). Further analysis of these data sets have revealed a possible two-mode structure of the inner fast solar wind (Bisi, 2006; Bisi *et al.*, 2007a) and thus this warrants further investigation. EISCAT was later enhanced with the building of the EISCAT Svalbard Radar (ESR) observing at 500 MHz (Wannberg *et al.*, 1997), and EISCAT then upgraded to 1420 MHz as an alternative observing frequency on two of its three sites on the mainland (Wannberg *et al.*, 2002). In addition, these same two mainland sites have had the UHF ~930 MHz receivers replaced with VHF 224 MHz receivers in 2012–2013.

In 2002, 2004, 2005, and again in 2006, observations were made using the Multi-Element Radio-Linked Interferometer Network (MERLIN) facility (Thomasson, 1986) with IPS observing frequencies of either 5 GHz or 6 GHz as well as at

1420 MHz. Canals (2002) states that the Very-Long-Baseline Array (VLBA) has also been used at 22 GHz for observations of IPS. There have been combined programs of MERLIN and EISCAT to probe the acceleration region of the solar wind and also to look in more detail into the large-scale structure of the solar wind and in particular, the direction of flow of the solar wind where non-radial flows have been detected (e.g., Moran, 1998; Moran *et al.*, 1998; Breen *et al.*, 2006; Bisi, 2006; Bisi *et al.*, 2007b; Breen *et al.*, 2008; Dorrian *et al.*, 2013) and the possible two-mode structure of the inner polar fast solar wind (Bisi, 2006; Bisi *et al.*, 2007a). The VLBA at 22 GHz has the capability of observing the solar wind as close as 2.5 $R_\odot$ (Klinglesmith, 1997), and MERLIN as close as 5 $R_\odot$ (Canals, 2002) at 5 GHz.

IPS is also very capable of detecting the passage of a coronal mass ejection (CME) through the inner heliosphere (e.g., Gothoskar and Pramesh Rao, 1996; Ananthakrishnan *et al.*, 1999; Jones *et al.*, 2007; Tokumaru *et al.*, 2007; Bisi *et al.*, 2009b; Tappin and Howard, 2010; Glyantsev *et al.*, 2015; and references therein). Indeed, Jackson (1984) was one of the first papers linking CME signatures in IPS data with the white-light CMEs as seen in coronagraphs at the time.

Multiple IPS-capable systems are still in use and under development around the world today over half a century after its first use as a method of probing inner-heliospheric outflows and structure. Single-site systems include the Ootacamund (Ooty) Radio Telescope (ORT) in India, the Big Scanning Array (BSA) at Pushchino in Russia, the Ukrainian T-shaped Radio telescope – second modification (official abbreviation UTR-2) near Hrakovo in Ukraine, the MEXican Array Radio Telescope (MEXART) in Coeneo, Michoacán, in Mexico, the Korean Space Weather Center (KSWC) IPS array on Jeju Island in the Democratic Republic of Korea (South Korea), and the Miyun Synthesis Radio Telescope (MSRT), Urumqui radio telescope, and the Miyun radio telescope, all located in China. Multi-site systems include the aforementioned EISCAT/ESR joint system (four sites in all), the aforementioned 327-MHz ISEE IPS arrays in Japan (originally four sites, now three), and the LOw Frequency ARray (LOFAR) centered in the Netherlands with international sites across central and western Europe (many Netherlands sites with, presently, nine international stations and three more to start construction). In addition, as a single-site system based on LOFAR technology and as a test bed for the future EISCAT_3D planned system, there is the Kilpisjärvi Atmospheric Imaging Receiver Array (KAIRA) which can be considered as a reconfigured LOFAR Netherlands non-core station. There are systems with other *ad hoc* IPS capabilities such as the Giant Metrewave Radio Telescope (GMRT) near Pune in India, the VLBA across the USA and the US Virgin Islands, the European Very Long Baseline Interferometer (EVLBI) Network (EVN), and the Millstone Hill Steerable Antenna (MISA) located at the MIT Haystack Observatory in Westford Massachusetts in the USA for example. Finally, the Murchison Widefield Array (MWA)

in Western Australia has, serendipitously, recorded its first observation of IPS with planning underway for some short, dedicated IPS test experiments as well as IPS capabilities to be tested with the Long Wavelength Array (LWA) in the USA (S. M. White, private communication, 2015).

13.6.2 An overview of IPS theory

Variations in the local refractive index of the interplanetary medium are the foundations for the IPS detected in the radio signals. These inhomogeneities have a characteristic scale size of tens to a few hundreds of kilometers. The irregular changes of refraction bend the radio waves in varying directions and so they then reach the observer from different directions. The refracted waves then combine with others causing constructive and destructive interference in the form of amplitude variations in the received signal (amplitude scintillation). The frequency of the fluctuations is about 0.5 Hz when detected from the ground (Hewish, 1989). Only if the patterns have a sufficient coherence (i.e., when the angular diameters are less than around 0.5 seconds of arc) will the scattered waves then combine to form a diffraction pattern. This diffraction pattern then drifts over the ground to give rise to the fluctuations in intensity (Ekers and Little, 1971; Coles and Harmon, 1978) as can be seen in Fig. 13.1.

Solar-wind parameters can be obtained from single-site analyses of a power spectrum of an observation of IPS (e.g., Manoharan and Ananthakrishnan, 1990; Aguilar-Rodriguez *et al.*, 2014), but more-robust methods are generally based on the cross-correlation of two simultaneous observations of the same radio source (e.g., Coles, 1996; Breen *et al.*, 1996a; Fallows *et al.*, 2008; Bisi *et al.*, 2010b; Fallows *et al.*, 2013). Figure 13.2 provides a simplified overview of a multi-site IPS experiment. The two observations are typically at the same observing frequency from both receivers; however, Bisi (2006) and Fallows *et al.* (2006) have shown that multi-frequency cross-correlations are also possible, and much science can still be achieved through such.

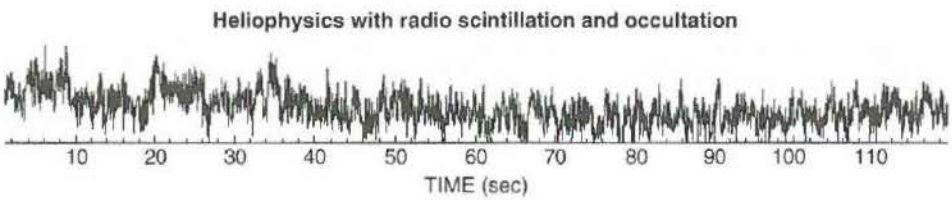

Fig. 13.1 Intensity fluctuation seen in a single observation of IPS using the Sodankylä site during an EISCAT observation on 05 September 2004 with radio source J1256-057 (3C279). (Adapted from Bisi, 2006.)

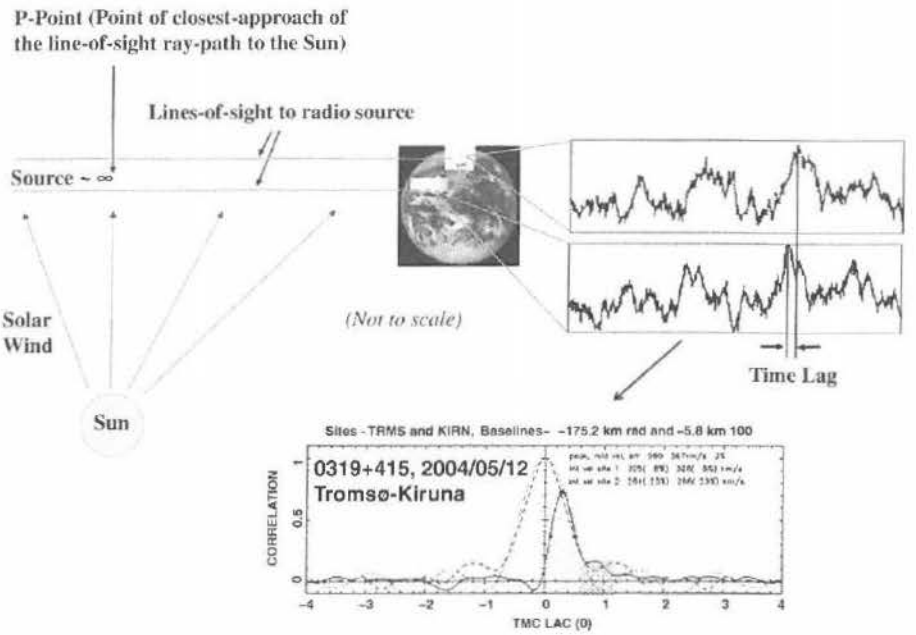

Fig. 13.2 The basic principles of multi-site IPS (in this case two EISCAT radar antennas, Tromsø and Kiruna) through the simultaneous observation of a single radio source as described in the text. The signal's amplitude variation is directly related to turbulence and density variation in the solar-wind outflow crossing the line of sight (LOS). A cross-correlation analysis of the two simultaneous signals received yields what is known as a cross-correlation function (CCF) which can be used as a first estimate of the velocities crossing the LOS. (Adapted from Bisi *et al.*, 2010b.)

The variations in the received signal at Earth depend on the structure of the solar-wind plasma through which it traverses. The IPS of the radio waves causes a 2D (two-dimensional) interference pattern across the Earth's orbit. As the irregularities casting the intensity pattern are moving out in the solar wind away from the Sun, a receiver on Earth will see the apparent intensity of the source varying on time scales of between ~0.1 s and 10 s. Fluctuations can become smooth due to minima from one part of the source overlapping with minima from another part. This depends on frequency and on distance from the Sun because the irregularities are larger further out from the Sun because of their natural expansion and the approximate decrease in density squared with increasing distance from the Sun. A simple formula for working out if a radio source is too large, is whether or not a source subtends an angle $\theta_s \geq L/D$, where L is the average size of the irregularity of solar wind, and D is the distance from the observer. If the radio source size on the sky is larger than $\sim\theta_s$, then the amplitude fluctuations will be smoothed out and no IPS will occur.

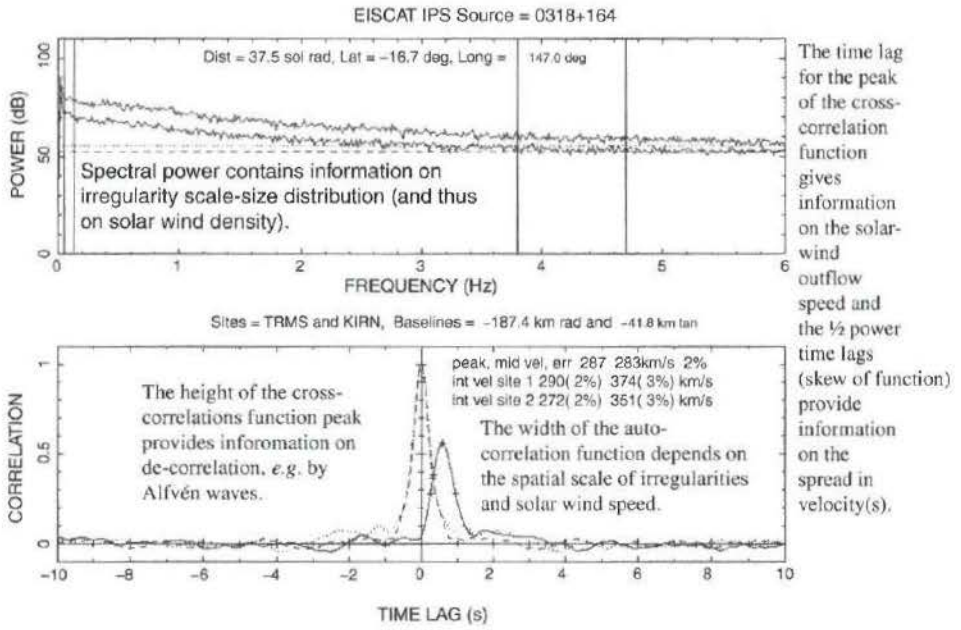

Fig. 13.3 The top plot displays an example Fourier-transformed spectrum from the two time series of a multi-site observation of IPS with EISCAT. The bottom plot shows a CCF of this observation. The vertical lines on the power spectrum to the left are the high-pass filters for each of the two sites and similarly to the right are the low-pass filters for each of the two sites. (Courtesy of R.A. Fallows.)

Figure 13.3 provides an example of the Fourier-transformed IPS power spectrum on a log–linear scale as well as a cross-correlation function (CCF) from an EISCAT observation of IPS with radio source J0318+164 (CTA21). Figure 13.4 provides an additional example of an IPS power spectrum on a log–log scale where features are more-clearly marked.

Ionospheric scintillation is also possible as already noted. This generally occurs with larger source sizes than IPS (because D is much smaller, so θ_s larger). Typical IPS time scales of 0.5 Hz are significantly faster than those of ionospheric scintillation. In addition, the diffraction of about 200 km of ionosphere is considerably large (likely due to the larger electron column density) so that high-frequency IPS is not normally confused with any effects that could come from the ionosphere (Hewish, 1989) unless there are very rapid flows in the ionosphere (private communication to A. R. Breen, 1995, as cited in Canals, 2002, and Bisi, 2006) where ionospheric scintillation may rise above a frequency of 0.2 Hz as seen in the power spectrum (A. R. Breen, private communication, 2005). In these cases, the ionospheric contribution may be seen as an extra bulge in the spectrum close to the low-frequency cut-off end of the IPS spectrum where there is a high-pass filter

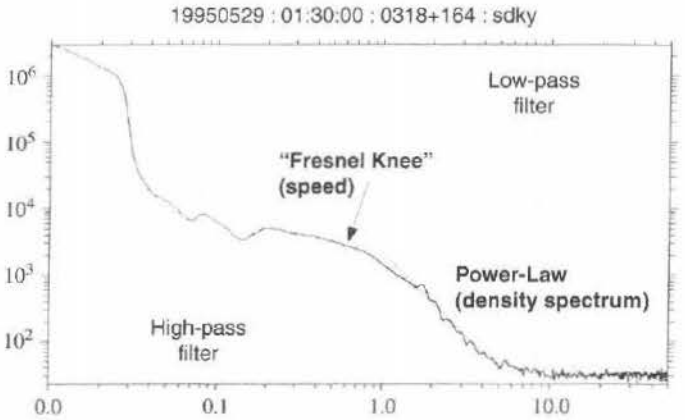

Fig. 13.4 An example IPS power spectrum on a log–log scale. The aforementioned low- and high-pass filters are more-clearly illustrated and individually labeled. The Fresnel knee is related to the speed/velocity of the solar-wind outflow, and the power law is related to the density. (Courtesy of R.A. Fallows.)

placed in the analyses. A low-pass filter in the analyses removes the background white noise from the higher-frequency end of the spectrum. At lower observing frequencies, the ionosphere can become more dominant and great care then needs to be taken to adequately filter out the ionospheric scintillation (where possible) or to not trust the validity of that observation, particularly for receivers at the Earth's high geomagnetic latitudes where ionospheric turbulence and variations in density are much greater. This has become prevalent in test observations of IPS using both KAIRA and the two new EISCAT 224 MHz remote sites.

The variations in the local refractive index are directly proportional to the density of electrons provided the variation in the electron density is small enough (Hewish, 1989). Using the notation of Uscinski (1977) and adapted from Fallows (2001), Canals (2002), and Bisi (2006), the refractive index, $n(x, y, z)$, can be described by the following set of equations starting with Eq. (13.1), where n_0 is the mean refractive index, $n'(x, y, z)$ is the variation of refractive index about the mean (above and below the mean refractive index), μ is the standard deviation of $n'(x, y, z)$, and $n_1(x, y, z)$ is the scaled form of $n'(x, y, z)$ with unit standard deviation:

$$n'(x, y, z) = \mu n_1(x, y, z) = n(x, y, z) - n_0. \tag{13.1}$$

The variation in refractive index is determined by the relative electron permittivity, ϵ, of the medium, i.e., the solar wind in this case. In the absence of particle collisions (the solar wind is a collisionless plasma), and if the magnetic field is of no concern (a simplification), this can then be represented by

$$\epsilon = n^2 = 1 - \frac{f_p^2}{f^2}, \tag{13.2}$$

where f_p is the plasma frequency (in Hz) and f is the observing frequency of the observation of IPS:

$$f_p^2 = \frac{N_e e^2}{4\pi^2 \epsilon_0 m_e}, \tag{13.3}$$

where N_e is the electron number density (in m^{-3}), ϵ_0 is the permittivity of free space ($8.854 \times 10^{-12}\,\mathrm{F\,m^{-1}}$), e is the electric charge of the electron ($-1.602 \times 10^{-19}\,\mathrm{C}$), and m_e is the mass of the electron ($9.109 \times 10^{-31}\,\mathrm{kg}$).

Because $f_p \ll f$, the refractive index can be written using a Taylor expansion, neglecting terms beyond first order:

$$n = 1 - \frac{1}{2}\frac{f_p^2}{f^2}, \tag{13.4}$$

so that

$$n' = \left[1 - \frac{N_e e^2}{8\pi^2 \epsilon_0 m_e f^2}\right] - \left[1 - \frac{\langle N_e \rangle e^2}{8\pi^2 \epsilon_0 m_e f^2}\right] = \frac{\delta N_e e^2}{8\pi^2 \epsilon_0 m_e f^2}, \tag{13.5}$$

where $\langle N_e \rangle$ is the average electron density at the P-point (the point of closest approach of the LOS to the Sun). The weighting contributions about the P-point along with the weighting function are illustrated in Fig. 13.5 and further description can be found later in this sub-section and in the next.

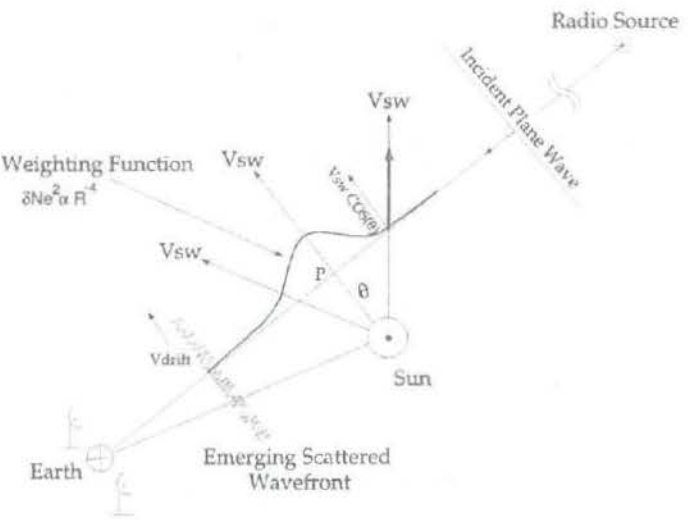

Fig. 13.5 The geometry of observations of IPS and how the weighting of scintillation potential along the LOS from the radio telescopes to the source varies due to the solar wind flowing across the LOS at different angles. (From Grall, 1995.)

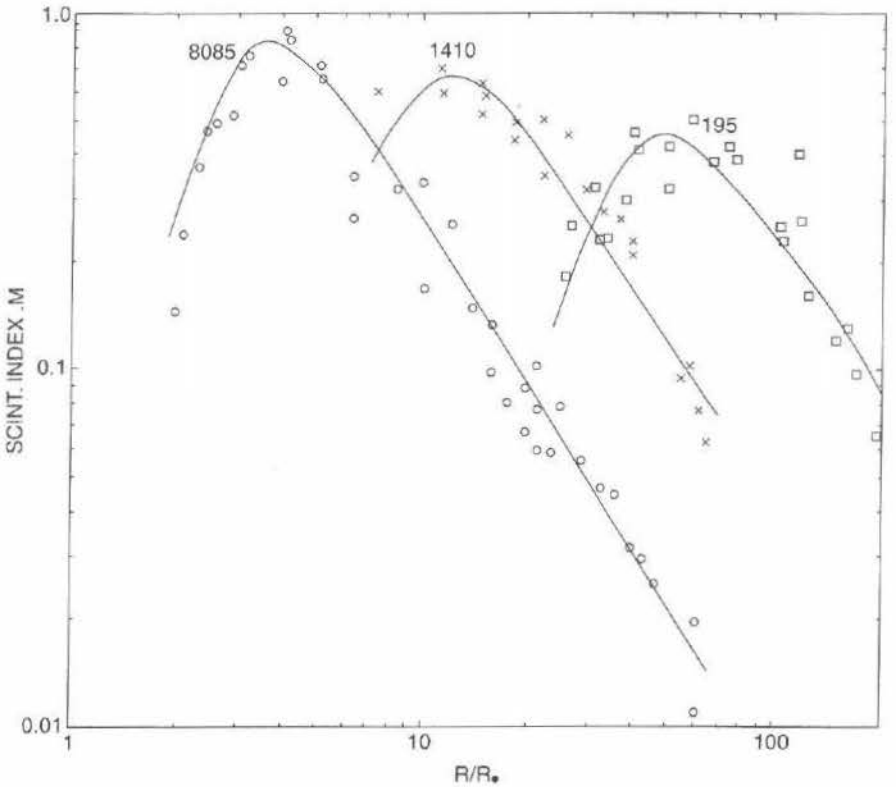

Fig. 13.6 A log–log plot showing for three different IPS observing frequencies of 8085 MHz, 1410 MHz, and 195 MHz, the scintillation index (m) response with distance from the Sun (in units of solar radius R_{Sun}). The scintillation index is the square of the scintillation power received at the antenna while observing a particular radio source. As illustrated by the figure, the higher the observing frequency, the closer-in to the Sun the peak in the scintillation index occurs and hence higher observing frequencies can be used to enable observations in the weak-scattering regime closer-in to the Sun as described by the earlier equations. (Reproduced from Coles, 1978.)

For observations closer-in to the Sun, N_e is larger and it is therefore assumed that δN_e is also increased and also the scale sizes of the irregularities are decreased (e.g., Fallows, 2001, and references therein). Hence, n' increases as the strong scattering regime is reached. Because n' is inversely proportional to the observing frequency squared, a higher observing frequency allows observations in the weak scattering regime to be made closer-in to the Sun than that of a lower observing frequency, as seen in Eq. (13.5) and Fig. 13.6. In contrast, as n' decreases with distance from the Sun, so does the scintillation level (amplitude) of the observation and a point is reached where the IPS amplitude variations become swamped with noise from the observing system. IPS is a capable method of observing the solar wind over a very

wide range of distances, especially if multiple frequencies are at the observer's disposal.

In weak scattering, when the variation between the phase changes is much less than one radian, the detected scintillation pattern can be treated as a linear sum from all the scattering events along the LOS from the source to the receiver. Diffraction of the radio waves can be thought of as occurring at a series of "thin screens" and the phase variations that are introduced by diffraction at any single "screen" build up into amplitude variations over a distance which is then dependent on the actual size of the density variations in that particular "screen". In strong scattering, however, this is not at all the case. Although analysis of the IPS results is still possible – as demonstrated by Imamura *et al.* (2014) and references therein – the amount of reliable information that can be extracted from the results is considered to be vastly reduced. The variation in refractive index (and thus for phase change) is shown by Eq. (13.5). It shows that the variation in phase change will be reduced if the observing frequency is increased and that the transition from weak to strong scattering therefore occurs closer to the Sun at greater observing frequencies (Fallows, 2001; Fallows *et al.*, 2006; Bisi, 2006). If the strong scattering regime is reached, then a sudden drop in the scintillation index occurs as is demonstrated by Fig. 13.6 where, for each of the three example frequencies shown respectively, as the P-point gets closer-in to the Sun, the scintillation index increases to a maximum before turning over and decreasing again, signifying the change of regime from weak to strong scattering for each example frequency.

13.6.2.1 Details of multi-site IPS and further IPS theory

Figure 13.5 (from Grall, 1995) shows the IPS scintillation potential and observing geometry along the LOS from the Earth to the distant point-like radio source. This figure takes into account the $\cos\theta$ effect for the foreshortening of the velocity crossing the LOS (because IPS is sensitive to the perpendicular component of velocity across the entire LOS).

Multi-site IPS is capable of providing a much more accurate determination of the solar-wind velocity (and other parameters) in general compared to a single-site observation of IPS. As already described, the radio waves scintillate due to the solar wind and cause a 2D pattern that drifts across the Earth due to the density irregularities in the solar wind flowing outwards from the Sun. Only if the alignment of the radio source, solar wind, and telescopes is such that the two receivers lie in the same plane which passes through the center of the Sun can the time lag between the signals recorded be used to derive the velocity, or velocities (depending on whether there are one or more streams crossing the LOS), flowing over the LOS. Observations of IPS are henceforth used as a tracer of the solar-wind outflow, and can be

used to study the evolution of the solar wind structure throughout interplanetary space (e.g., Canals, 2002; Bisi, 2006).

One can also use IPS to determine the direction of outflow because of the nature of where the maximum peak in the CCF occurs compared with the radial direction of flow, and it can indicate non-radial flows in the meridional direction (e.g., Moran, 1998; Moran *et al.*, 1998; Bisi *et al.*, 2005; Breen *et al.*, 2006; Bisi, 2006; Breen *et al.*, 2008; Bisi *et al.*, 2010a). The time lag, δt, can be used at maximum correlation along with the information on the component of the baseline length measured parallel, the parallel baseline (B_{Par}), to the Sun–Earth line to give, to a first approximation, the velocity of the primary/dominant stream of solar wind flowing across the lines of sight. As the Earth rotates, the geometric baseline between the two observing sites projected onto the sky also rotates making the long side of a right-angled triangle (from the point of view of the radio source). The outflow of plasma makes one side of the triangle, B_{Par} between the two observing antennas lies along this outflow direction, and finally, the third side is as a result of the angle between B_{Par} and the projection of the geometrical baseline completing the right-handed triangle, is the perpendicular baseline (B_{Perp}) (which for a cross-correlation is usually significantly smaller than the length of B_{Par}). The initial velocity estimate is accomplished by using Eq. (13.6), where the term *Distance* in the equation refers to the length of B_{Par} (which, for completely radial outflow, would result in maximum cross-correlation when B_{Par} lies completely along the radial direction with no perpendicular component):

$$v_{\mathrm{SW}} = \frac{Distance}{\delta t}. \tag{13.6}$$

This equation can also be used for the time lag of other peaks (if any) that appear in the CCF. Observations of IPS contain contributions from the whole of the LOS, but are only sensitive to the perpendicular component of velocity across the LOS as already noted. The aforementioned cos θ effect will therefore cause a broadening of the CCF and will lead to an underestimation of the velocity of the solar-wind stream(s) detected crossing the LOS. The maximum scattering will occur in a region along the LOS around the P-point of the LOS (again, see Fig. 13.5) because the scattering potential of the solar wind decreases with increasing distance from the Sun for a given frequency within the weak-scattering regime (again, see Fig. 13.6) as well as the perpendicular component across the LOS becoming progressively smaller. To a first approximation, this is $\propto 1/R^4$, which shows that the majority of the scattering occurs at the P-point (where $\cos\theta \simeq 1$). Hence, by a rough correction, the IPS results can be corrected by a multiplication of 1.18 (Breen *et al.*, 1996b), although more thorough methods of velocity calculation are usually undertaken (e.g., Coles, 1996; Fallows, 2001; Bisi, 2006; Fallows *et al.*,

2006; Jones, 2007; Jones *et al.*, 2007; Fallows *et al.*, 2008; Bisi *et al.*, 2010a,b; Fallows *et al.*, 2013).

Equation (13.8) shows the temporal power spectrum under weak scattering conditions, where r_e is the classical electron radius

$$r_e = \frac{1}{4\pi\epsilon_0}\frac{e^2}{m_e c^2} = 2.818 \times 10^{-15}\text{m}, \tag{13.7}$$

λ is the observing wavelength, α is the power-law exponent (e.g. Kolmogorov), v_p is the component of solar wind velocity perpendicular to the line of sight, q is the 2D spatial wavenumber (normally in $x-y$ coordinates), q_i is the inner-scale for turbulence (the scale at which the turbulence dissipates), z is the distance from Earth to the scattering "screen", θ_0 is the diameter of the source in radians, $v(q, z, \theta_0)$ is the visibility function of a radio source, ϵ_0 is the permittivity of free space, e is the charge of the electron, m_e is the mass of the electron, and c is the speed of light in a vacuum ($2.998 \times 10^8\,\text{m s}^{-1}$). It is described in its various forms by Salpeter (1967), Scott *et al.* (1983), Klinglesmith (1997), Moran (1998), Bisi (2006), Fallows *et al.* (2006), and references therein:

$$P(f) = 2\pi r_e^2 \lambda^2 \int_0^\infty \frac{2\pi}{v_p(z)} \int_{-\infty}^\infty 4\sin^2\left(\frac{q^2\lambda z}{4\pi}\right) |v(q, z, \theta_0)|^2 q^{-\alpha} \exp -\left(\frac{q}{q_i}\right)^2 R^{-4} dq_y dz. \tag{13.8}$$

The full development and derivation of the underlying steps to get to this equation can be found in Salpeter (1967).

The Fresnel filter, described by Eq. (13.9) acts as a high-pass filter attenuating wavenumbers below the Fresnel spatial frequency, q_f, as given in Eq. (13.10). The Fresnel filter is necessary because the wavefronts need a certain distance from the point of scattering to develop into a scintillation pattern – this is known as the Fresnel distance – and it is defined as the distance at which these wavefronts are again in phase and the amplitude variations first become "fully developed". Because of this, the diffraction of radio waves that occur very close to the observer (near the Earth) would thus not have time to fully develop from phase changes into amplitude changes and therefore would not contribute very much to the overall scintillation pattern received at the Earth from along the IPS LOS. This is also illustrated by the weighting along the IPS LOS as seen earlier in Fig. 13.5. This means that the cause of the scintillation along the LOS is slightly biased to the source side of the P-point along the LOS and not the Earth side, although the majority of the scintillation comes from around the P-point as already described. Additional details and exploration of the scintillation potential along the IPS LOS are described by Fallows (2001).

$$Fresnel\ Filter = 4\sin^2\left(\frac{q^2\lambda z}{4\pi}\right), \tag{13.9}$$

$$q_f = \sqrt{\frac{4\pi}{\lambda z}}. \tag{13.10}$$

The Fresnel radius, defined by Eq. (13.11) is that of the first Fresnel zone:

$$r_f = \sqrt{\lambda z}. \tag{13.11}$$

This gives a maximum scale size of the irregularities for which amplitude scintillation can occur; it is dependent on the observing frequency and the distance to the scattering "screen". For example, for an observing wavelength (frequency) of ~21 cm (1420 MHz), the maximum scale-size of irregularity at a "thin screen" of scattering at 1 AU is ~177 km; at ~32 cm (928 MHz), this is ~219 km; and at ~60 cm (500 MHz), it is ~300 km.

The $\exp[-(q/q_i)^2]$ term in Eq. (13.8) describes the turbulent dissipation towards smaller irregularity scales and it also attenuates the scintillation power spectrum at wavenumbers higher than q_i. The source visibility function also acts as a low-pass filter attenuating wavenumbers above:

$$q_s = \frac{1}{z\theta_0}. \tag{13.12}$$

13.6.2.2 Increasing baseline length for multi-site observations of IPS

The ability of observations of IPS to resolve streams of solar wind with different velocities increases as the radial separation in the plane of sky of the lines of sight increases (Klinglesmith, 1997; Moran *et al.*, 1998; Bisi *et al.*, 2005; Breen *et al.*, 2006; Bisi *et al.*, 2010b; Fallows *et al.*, 2013). However, the time lag between the two sites is increased by the increase in B_{Par} between the two observing sites and as the irregularity pattern is evolving in time; any increase in B_{Par} will thus lead to a decrease in the degree of correlation, although the length of time that coherency can be maintained is still yet to be studied in any detail (Klinglesmith, 1997; Moran *et al.*, 1998; Bisi *et al.*, 2005; Bisi, 2006; Breen *et al.*, 2006). Thus far, correlations over periods of around eight seconds have been recorded (Bisi *et al.*, 2005; Bisi, 2006; Breen *et al.*, 2006).

The effect of increasing B_{Par} for a particular observation can be seen in Fig. 13.7. As B_{Par} is increased, the correlation of the signal is decreased at the primary peak (the dominant solar wind flow velocity) and is transferred elsewhere within the CCF. A second peak (i.e., a second solar-wind flow) can be resolved if one is present when B_{Par} is long enough. Indeed, Bisi *et al.* (2007a), Breen *et al.* (2008), Fallows *et al.* (2008), and Bisi *et al.* (2010a) have shown that up to three streams

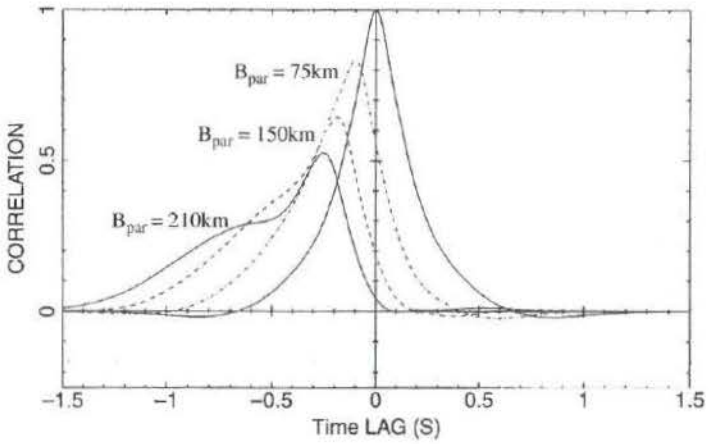

Fig. 13.7 The effect of increasing the parallel baseline (B_{Par}) of a multi-site observation of IPS on the CCF. (From Klinglesmith, 1997.)

can be resolved and subsequently determined in terms of their parameters and relative weighting factors between the differing streams present crossing the LOS.

The general approach of estimating the velocity of solar wind from the time lag does have some limitations, however. The most important of these is that a finite spread in solar-wind speeds across the stream considered will introduce a skew of the correlation function to shorter time lags, this time, leading in turn to an overestimate of the plane-of-sky speed (e.g., Breen *et al.*, 1996a).

The larger B_{Par}, the larger the B_{Perp} for a given angle relative to the solar wind outflow (θ):

$$\tan\theta = \frac{B_{\mathrm{Perp}}}{B_{\mathrm{Par}}}. \tag{13.13}$$

Thus, the likelihood of detecting any non-radial flow is increased if you use extremely-long-baseline (ELB) IPS (e.g., Bisi *et al.*, 2005; Breen *et al.*, 2006; Bisi, 2006; Bisi *et al.*, 2007b; Bisi *et al.*, 2010a) over shorter-baseline multi-site IPS alone.

13.6.2.3 Dual-frequency IPS

Equation (13.8) is suitable only for representing the CCFs for a single observing frequency. However, relatively simple modifications can be made to the equation to allow the cross-correlation of two different frequencies: one at each of the receivers used (Salpeter, 1967; Fallows *et al.*, 2006), or from the same site when observing at multiple frequencies or over a wide bandwidth. It is the terms involving λ^2 that split into two single λ_i terms (as per Fallows *et al.*, 2006, and also Bisi, 2006). The resulting Eq. (13.14) is taken directly from Fallows *et al.* (2006):

$$P(f) = 8\pi^2 r_e^2 \lambda_1 \lambda_2 \int_0^\infty \frac{2\pi}{v_p(z)} \int_{-\infty}^\infty \sin\left(\frac{q^2\lambda_1 z}{4\pi}\right) \sin\left(\frac{q^2\lambda_2 z}{4\pi}\right)$$

$$|v(q, z, \theta_0)|^2 q^{-\alpha} \exp - \left(\frac{q}{q_i}\right)^2 R^{-4} dq_y dz. \tag{13.14}$$

Observations of IPS are sensitive to density scales that can overlap, and so still provide meaningful correlation when the two different observing frequencies are not too far apart and while observing at both still remains in the weak-scattering regime for both observing frequencies. Fallows *et al.* (2006) have shown that observations of IPS at frequencies of 500 MHz at one receiver and 1420 MHz at another still provide meaningful IPS results – suggesting that different scale sizes of micro-structure within the solar-wind outflow move outward with the same velocity and hence are in line with the bulk velocity as measured in situ. The maximum scale size of a density irregularity of a range of scale sizes is more-specifically determined by the observing wavelength (or frequency) as defined earlier in Eq. (13.11). These multi-frequency correlations are still obtainable even over the very long baselines such as from the ESR to the EISCAT mainland sites, and also with the ELB observations between EISCAT and MERLIN sites using the Tromsø receiver recording at 928.5 MHz and all others at 1420 MHz (e.g., Bisi, 2006; Jones, 2007).

13.6.3 Three-dimensional computer-assisted tomography (CAT)

Many observations of IPS over several weeks or months will allow for the three-dimensional (3D) computer-assisted tomography (CAT) reconstruction of the detailed structure of solar-wind outflow throughout the inner heliosphere. Since the 1990s, a set of CAT techniques have been developed at UCSD. Here, we focus on the UCSD techniques that are used for both detailed science investigations as well as for real-time space-weather forecasting (see, e.g., http://ips.ucsd.edu/, http://www.spaceweather.go.kr/models/ips, and http://helioweather.net/models/ipsbd/vel3r1e1b/index.html).

The UCSD 3D CAT reconstructions use perspective views of solar co-rotating plasma (e.g., Jackson *et al.*, 1998, 2011b) and of outward-flowing solar wind and transient features (e.g., Jackson and Hick, 2005; Jackson *et al.*, 2011b) crossing the IPS observing lines of sight, and also with the inclusion of various near-Earth in-situ measurements directly into the time-dependent reconstructions (Jackson *et al.*, 2010b, 2013). Both velocity and density are obtained through the use of a kinematic solar-wind model based on the conservation of mass and mass flux in the heliosphere as structure propagates outwards with a radial-flow assumption from a model source surface at 15 $R_\odot$ out to 3 AU (or about 650$R_\odot$). Schematics showing

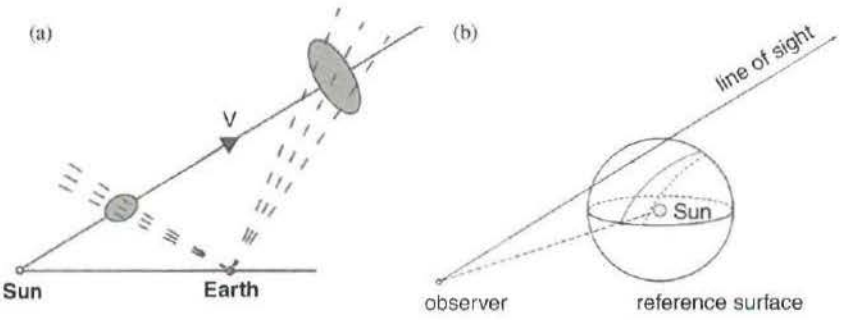

Fig. 13.8 The left-hand image (a) shows a schematic of the outward-flowing solar-wind structure which we know follows very specific physics as propagation away from the Sun takes place. By observing large areas of the sky with time, this allows individual features to be observed several times over time and this has the same effect as a moving detector in a comparable instantaneous time such as CAT scans used in medical imaging where sensors rotate around the body and not the body moving through the sensors in time. The right-hand image (b) depicts a schematic of how an individual IPS LOS maps/projects onto the source (reference) surface for use in the UCSD 3D CAT; the solid line is the immediate projection of the LOS to this surface and the dashed line is the projected location that takes into account the solar wind speed. (Adapted and combined from Jackson *et al.*, 2010a, 2011b.)

separately the overall perspective view as well as then how the projection of each LOS maps onto a source surface above the Sun are shown in Fig. 13.8.

The IPS lines of sight (or portions of each line of sight) are mapped onto the source surface for a particular region of interest, usually a Carrington rotation (CR) in length, before then being fitted iteratively to a best-fit solution. A display of the lines of sight onto two CR maps is shown in Fig. 13.9.

Using the IPS scintillation level converted to the disturbance factor level or normalized scintillation level, otherwise known as the g-level, as a proxy, the solar wind density can be inferred from observations of IPS in the 3D CAT reconstructions (e.g., Hick and Jackson, 2004; Jackson and Hick, 2005; Bisi *et al.*, 2007c; Breen *et al.*, 2008; Bisi *et al.*, 2009b; Jackson *et al.*, 2013). The 3D velocity reconstructions can take place directly from the IPS velocity determinations, however (e.g., Bisi *et al.*, 2007b, 2010c). For density, the g-level is defined by:

$$g = m/\langle m \rangle, \tag{13.15}$$

where, m is the observed scintillation level and $\langle m \rangle$ is the modeled mean level of $\Delta I/I$ for the source at its elongation and gain calibration at the time of its observation, for source-intensity variation, ΔI, and the measured signal intensity, I. As described in detail by Jackson and Hick (2005) and taken from Bisi *et al.* (2008c),

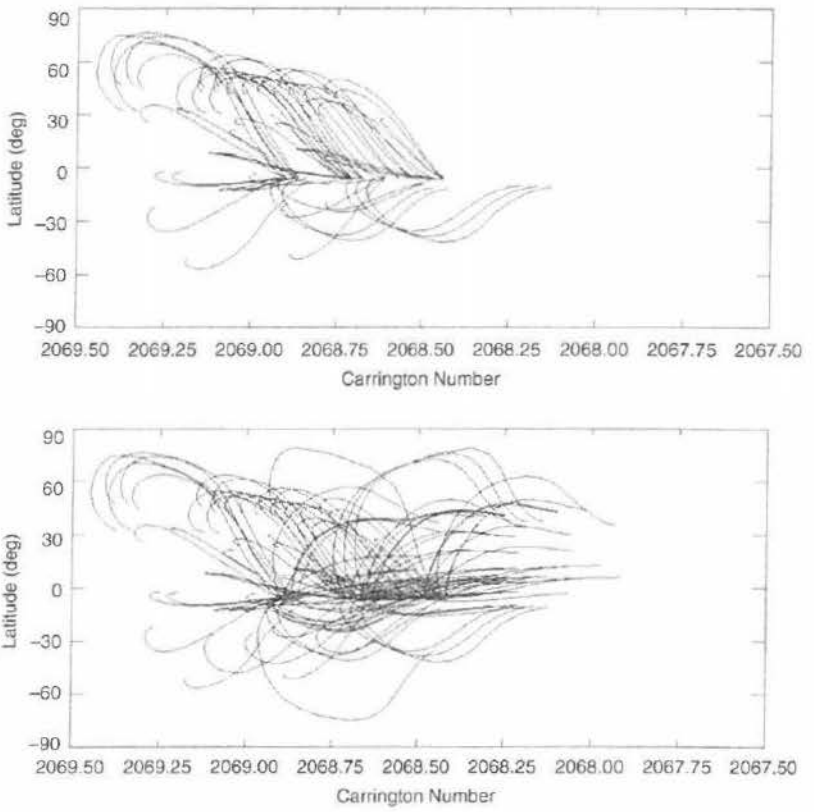

Fig. 13.9 The STELab IPS lines of sight used by the UCSD 3D CAT from g-level (top) and velocity (bottom) determinations from observations of IPS using the STELab system mapped back to the 15 $R_\odot$ source surface (lower boundary) in the UCSD 3D CAT. The display is over two Carrington rotations (CRs), and as can be seen, the velocity coverage is far greater onto these two CR maps used for the tomography (CR2067.50 to CR2069.50) than that of the g-level coverage in this particular example. The numbers of data points (lines of sight used) for velocity and g-level need not be the same and indeed often differ. (From Bisi *et al.*, 2009a.)

scintillation-level measurements have been available from STELab (now ISEE) since 1997 for example, but velocity determinations from much earlier.

The g-level proxy for density uses Eq. (13.16) because density values along a LOS are not known a priori but are assumed for small-scale variations with a power-law scaling of heliospheric density:

$$\Delta N_e = A_c R^\alpha N_e^\beta. \tag{13.16}$$

Here, A_c is a proportionality constant, R is the radial distance from the Sun, α is a power of the radial falloff, and β is the power of the density. The parameters A_c,

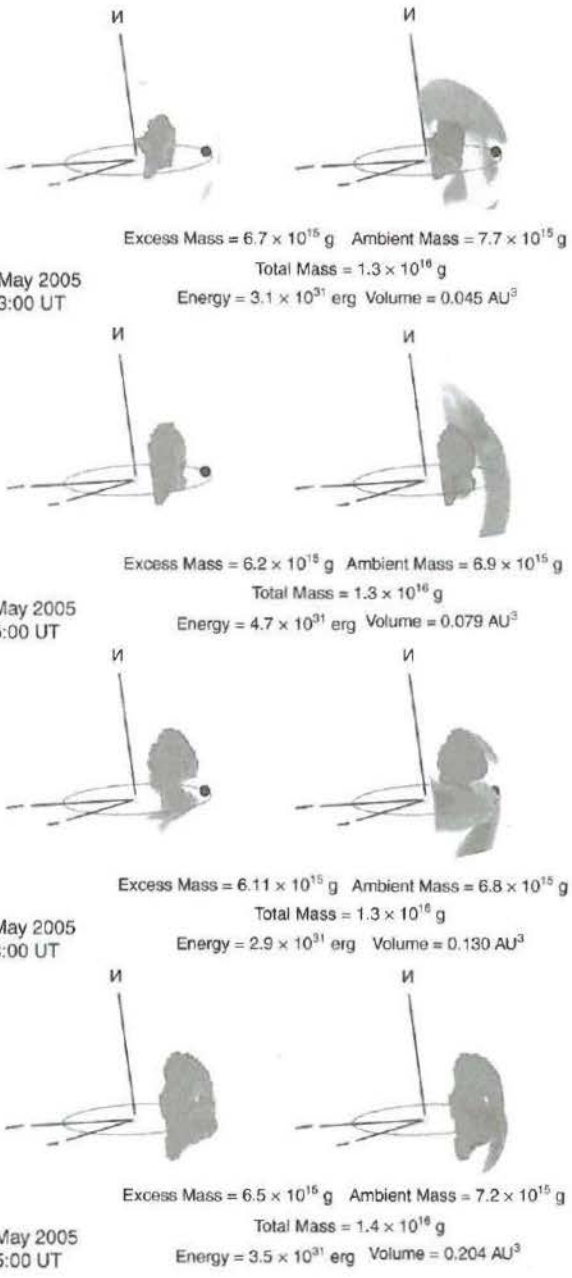

Fig. 13.10 The 3D CAT reconstructed visualization of the distribution of solar-wind density upwards of $8\,e^{-}\,cm^{-3}$ (brighter colors toward yellow mean increasing density) on the left-hand side and high-velocity portions (blue) on the right-hand side showing the developing and changing reconstructed structure of the 13–15 May 2005 coronal mass ejection (CME) event sequence. The left-hand density images are highlighted with green cubes to encompass the reconstructed volume of the mass portion of the CME. This same highlighted volume is depicted

α, and β are determined using best-fit comparisons with in-situ measurements at 1 AU. The values shown here are as previously used for 327 MHz IPS observations: A_c is set equal to 1, α is determined as -3.5, and β determined to be 0.7 (see Jackson *et al.*, 2003, for further details).

The UCSD 3D CAT reconstruction techniques can also be applied to the Thomson-scattered white-light observations from the Solar Mass Ejection Imager (SMEI) (Eyles *et al.*, 2003; Jackson *et al.*, 2004) with much-improved spatial and temporal digital resolution in density alone (e.g., Jackson *et al.*, 2008; Bisi *et al.*, 2008a,c; Jackson, 2011; Jackson *et al.*, 2011a,b; Yu *et al.*, 2014), and to IPS data from the ORT at an intermediate-level resolution for both density and velocity (e.g., Bisi *et al.*, 2009b). Similar much-improved-quality 3D IPS CAT reconstructions are expected from LOFAR and MWA (when the MWA becomes fully IPS capable), and eventually with the Square Kilometre Array (SKA) also. Plans are underway for the use of Solar TErrestrial RElations Observatory (STEREO) Heliospheric Imager (HI) data for input to the UCSD CAT to enable higher-resolution density reconstructions confined to a relatively-small volume along the Sun–Earth line. IPS can also be included with SMEI (or HI) data to allow for velocity to also be reconstructed alongside the density from SMEI (or HI). However, both the radio source size (angular size on the sky) and the observing frequency determine a weighting factor needed for the distribution of IPS contributions along each LOS. Generally, however, the greater the number of LOSs as input to the tomography, the higher the digital resolution and temporal cadence that can be achieved. In addition, these 3D reconstructions can be used to better constrain the analyses of the greater-sensitivity ELB observations of IPS by providing accurate contextual information on where streams/structures are located crossing the LOS (e.g., Breen *et al.*, 2006; Bisi *et al.*, 2007b; Breen *et al.*, 2008; Bisi *et al.*, 2010a).

Figure 13.10 (from Bisi *et al.*, 2010a; further details of this event and this set of images are given there) shows an example of some of the physical parameters that are able to be obtained from low-resolution UCSD CAT reconstructions (in this

---

Caption for 13.10 (cont.)

on the right-hand velocity reconstructions for illustrative purposes. Each image is labeled with the masses, volume, and energy values on each date and time as shown. All non-CME-related features have been removed for clarity of viewing when displaying the 3D volume. The axes are heliographic coordinates with X-axis direction pointing toward the vernal equinox, and Z-axis directed toward solar heliographic North. An r^{-2} density increase has been added to better-show structures further out from the Sun (the central sphere) to the Earth (the blue sphere) along with the Earth orbit (ellipse). (From Bisi *et al.*, 2010a.) A black and white version of this figure will appear in some formats. For the color version, please refer to the plate section.

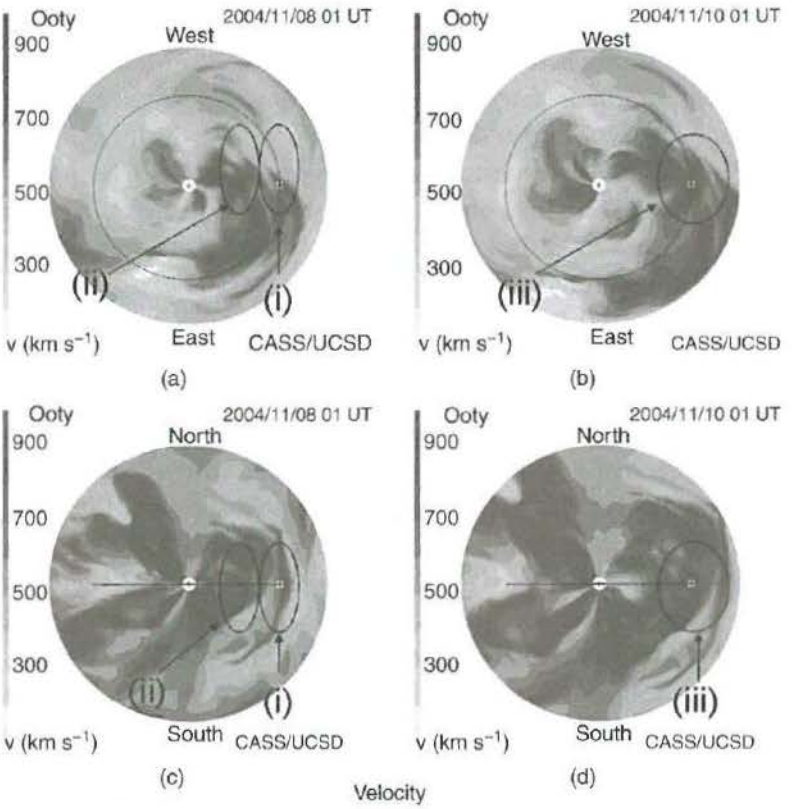

Fig. 13.11 Summary figure of the Ooty ecliptic, (a) and (b), and meridional, (c) and (d), cuts through the 3D velocity (this page) and density (next page) reconstruction out to 1.5 AU at the date and times shown. Various features are circled in the images which relate to various CME features from interacting CMEs which ultimately result in multiple geomagnetic storms at Earth; the in-situ time series from such are shown in Fig. 13.12. Earth's orbit is shown as a near-circle or line with the Earth, $\oplus$, indicated on each panel. Velocity contours are shown to the left of each of the four velocity images and similarly those are also given for the density cuts. These are prime examples of how the IPS CAT can work for interacting CMEs through the inner heliosphere. (From Bisi *et al.*, 2009b.)

case, $20° \times 20°$ digital resolution in latitude and longitude with 0.1 AU distance increments from the Sun on a daily cadence broken into six-hourly interpolations – typical resolutions used for STELab or EISCAT IPS data), or at a higher resolution showing many more detailed features as in Fig. 13.11 (taken from Bisi *et al.*, 2009b, where a more-in-depth discussion and explanation of these labeled features are given) using IPS data from Ooty (at a higher $10° \times 10°$ digital resolution in latitude and longitude with 0.1 AU distance increments from the Sun on a half-daily cadence broken into three-hourly interpolations). In addition, Fig. 13.12 shows an

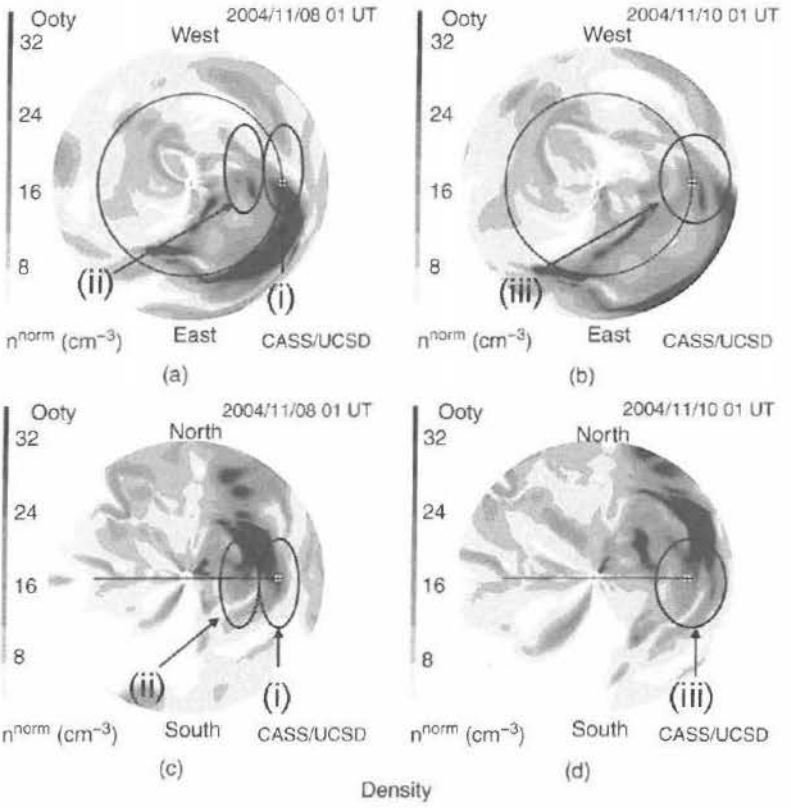

Fig. 13.11 (cont.)

in-situ time series extraction from both the velocity (top) and density (bottom) as compared with the hourly-averaged in-situ measurements recorded by the Wind spacecraft. As with Fig. 13.11, a detailed description of these labeled features in Fig. 13.12 is given in Bisi *et al.* (2009b).

13.6.4 The future of space weather science and forecasting: the IPS contribution to heliophysics

As a reminder, one of the strongest points of the IPS technique is that it enables us to make global observations of the inner heliosphere including a high coverage of the polar regions that are inaccessible to in-situ measurements until another out-of-ecliptic spacecraft mission becomes available, as well as within a large range of distances out from the Sun (from as near as a few $R_{\odot}$ to around 3 AU from Sun center – which includes the near-Sun regions inside the orbits of Mercury and Venus). The global observations of the solar wind in this current solar cycle (Cycle 24) are particularly valuable from the viewpoint of response to peculiar

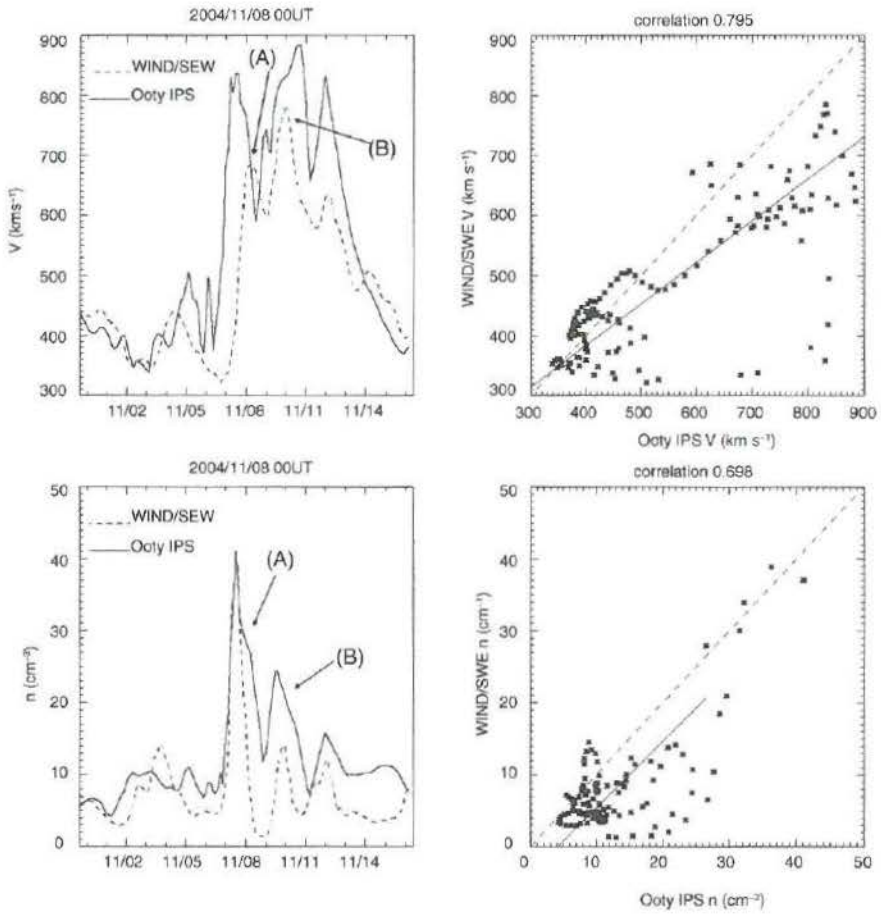

Fig. 13.12 The top-left plot compares the velocity time series at the Wind spacecraft extracted from the Ooty IPS reconstruction (solid line) with Wind solar wind velocity measurements (dashed line), and similarly the bottom-left plot for Wind density measurements. Both the Wind spacecraft velocity and density data are hourly-averaged data that were further averaged with a half-daily cadence to match that of the 3D reconstruction cadence. The top-right plot shows a scatter diagram for the two data sets for velocity, and similarly the bottom-right plot for density; the dashed line on each correlation plot is for a 100% correlation while the solid line shows the best-fit of the data here. (A) and (B) on the left-hand plots relate to features also highlighted earlier in Fig. 13.11. (From Bisi *et al.*, 2009b.)

solar activity (perhaps signifying an exit from a period of grand maxima) and also from the viewpoint of crucial information to interpret Voyager measurements at the outer boundary region of the heliosphere (M. Tokumaru, private communication, 2015).

IPS has been shown to be able to detect Earth-directed CMEs, CMEs with a glancing blow on the Earth, and CMEs elsewhere throughout the inner heliosphere

(e.g., Manoharan *et al.*, 2000; Fallows, 2001; Breen *et al.*, 2006; Jones, 2007; Jackson *et al.*, 2007; Jones *et al.*, 2007; Breen *et al.*, 2008; Bisi *et al.*, 2008b; Bisi *et al.*, 2010a, d; Jackson, 2011; Jackson *et al.*, 2011b; and references therein) making it a technique with improved proven potential for space-weather studies and for studying Earth-directed events with its forecasting capabilities continuously being advanced through new analyses and modeling techniques (e.g., Jackson *et al.*, 2013; Bisi *et al.*, 2014; Aguilar-Rodriguez *et al.*, 2014; Jackson *et al.*, 2015a, b; Aguilar-Rodriguez *et al.*, 2015; Jian *et al.*, 2015; and references therein).

It may be possible for multi-site observations of IPS to provide a way of directly estimating the magnetic-field direction of the plasma outflow from the Sun, at least when observing certain solar-wind/transient conditions. Under some circumstances, usually during an observation of a CME, the CCF displays a negative lobe near to or at the zero time lag (e.g., Klinglesmith *et al.*, 1996; Klinglesmith, 1997; Jones *et al.*, 2007; Bisi *et al.*, 2014). Most, if not all, CMEs are now considered to contain magnetic flux ropes that are ejected from the Sun (N. Gopalswamy, private communication, 2013). The density irregularities giving rise to IPS are therefore expected to be anisotropic, usually assumed to be "cigar-shaped" with the long axis parallel to the interplanetary magnetic field. In the regular solar wind, this elongation in the irregularities is usually parallel to the solar wind flow along the outflow direction (approximately radial in direction from the Sun). Modeling of the spatial correlation function by Klinglesmith *et al.* (1996) relates the negative lobe seen in IPS CCFs to the rotation of density irregularities such that their long axis is now more perpendicular to the solar-wind outflow, thus indicating rotation of the magnetic field relative to this flow. Whilst this has often been used as a signature that a CME is likely to be present crossing the LOS, no attempt (thus far) has been made to relate this more precisely to the magnetic-field rotation itself, or to use observations of IPS to sample the spatial correlation function in order to more-directly assess the irregularity orientation in detail.

In order to estimate the orientation of density irregularities in the solar wind, multi-site observations of IPS are required to form different CCFs with different baseline lengths and B_{Par} orientations relative to the plasma outflow. LOFAR has the distinct advantage for such an investigation of the CCF due to the large number of widely spaced stations that allow the spatial correlation function to be sampled in single, short observations, while increasing these numbers further with the inclusion of simultaneous observations of IPS with EISCAT and/or KAIRA much further north in geographic latitude.

Recent LOFAR and KAIRA test observations of both IPS and ionospheric scintillation have enabled the simultaneous observing of well over ~80 MHz in

bandwidth. This allows for the creation of dynamic spectra to investigate the scintillation at all observing frequencies and to study the type of scattering and the transition from weak to strong scattering for a particular observation of IPS precisely where this transition occurs for each observation.

In addition, when simultaneous observations of IPS are undertaken at a range of observing frequencies, say f to $6f$ (say, 40 MHz to 240 MHz – a capability of LOFAR now with the exception of the commercial FM band and a small band higher up in frequency), such data would be extremely useful in examining the scale size of the density irregularities responsible for IPS, and the shape of the density and cross-frequency spectra (e.g. Liu and Peng, 2010). It is also very useful for studying the transition between weak and strong scattering of the interplanetary medium and to extract the physical properties of the solar wind (P. K. Manoharan, private communications, 2013, 2015). The correlation between multiple observing frequencies can also provide the effective scale size of IPS in the solar wind and can identify the phase coherence as a function of the size of the irregularities. In the case of a propagating radio burst (e.g., type-III solar radio-burst emission, cf., Chs. 4 and 5 in Vol. III), from low to high coronal heights (generally, higher to lower frequencies as the source region propagates out from the Sun), the scattering by random density fluctuations plays an important role in increasing the angular width of visibility of radio emission with respect to the center (or direction) of the electron beam causing the emission. In other words, this scattering distorts the characteristics of the frequency of solar radio bursts. The smallest scale size of density irregularities in the case of IPS, the cut-off scale or inner-scale size (e.g., Coles and Harmon, 1978) present in the solar wind will determine the typical scale size of type-III radio emission.

The IPS of individual radio sources gives information on the small-scale density turbulence level and the solar-wind speed crossing the LOS in the direction of the radio source. The nature of the turbulence changes depending on the features crossing over the LOS and this is reflected in the spectrum (e.g., Coles and Harmon, 1978, 1989; Manoharan *et al.*, 2000). The study of the scintillation turbulence aspect of IPS has also had relevance much further afield, such as in the detection of submarines using sonar buoy arrays, and in providing laser-guided bombs (B. V. Jackson, private communication, 2015).

The IPS information is also important for the problem of coronal sources of the solar wind streams with different properties as well as for solar-wind acceleration. The IPS information, in particular about the solar-wind-speeds spatial distribution, can be used as initial conditions in the problem of the outer-heliosphere modeling. Further investigations into the solar-wind acceleration regions are open to higher-frequency ($\sim$1420 MHz and higher) observations of IPS probing close-in to

the Sun (the inner-most part of the heliosphere right down to the low corona well inside coronagraph fields of view). This, coupled with recent work on velocities obtained from coronal imaging (e.g., Jackson *et al.*, 2014; and references therein), paves a way to investigate precisely where the solar-wind acceleration takes place and to help pin down methods by which the solar wind undergoes this acceleration. This also allows another method of studying the possible bi-modal nature of polar fast solar wind as a result (noted earlier) of IPS and Ulysses investigations carried out by Bisi *et al.* (2007a).

The comparison between the data on small-scale density turbulence, from one side of IPS capabilities, and the large-scale density and other plasma parameters measured by in-situ and spacecraft radio occultation methods, from the other side, show that IPS is important for the problem of the physical nature of the solar-wind plasma turbulence and for the problem of connection between the mean solar-wind parameters and the statistical turbulence parameters throughout the inner heliosphere (I. Chashey, private communication, 2015).

More recently, the UCSD IPS 3D CAT has been shown to be able to successfully combine the current-sheet source surface (CSSS) field modeling (Zhao and Hoeksema, 1995a,b) with the velocity information gleaned from the IPS to provide a system that allows the extrapolation upward of closed fields from near the solar surface (Jackson *et al.*, 2015a). This method allows for the comparison of the north–south component of magnetic fields to be investigated and compared with near-Earth in-situ measurements for solar-minimum conditions. It has successfully been tested for two recent CME case studies with much success (3–5 January 2015 stream interaction region (SIR) and the 7–8 January 2015 CME, as well as the St. Patrick's Day 2015 CME events), and provides a potentially viable near-future method of forecasting the southward component of the magnetic field benefiting greatly from the incorporation of IPS data.

Finally, Jian *et al.* (2015), conducted a survey of the current coronal and heliospheric models that are hosted and run at NASA's Community Coordinated Modeling Center (CCMC). A total of 10 model runs were carried out for the coronal/heliospheric modeling with results from the UCSD 3D CAT matching the best overall with observed time series of velocity and density. These modeled values also work best for SIRs (including the recurring co-rotating interaction regions or CIRs) throughout seven solar (Carrington) rotations modeled in 2007 (around the time of solar minimum). This matches well with the prospects and recent results discussed by Bisi *et al.* (2014) and also by Jackson *et al.* (2015a) for the IPS-driven ENLIL model (ENLIL is a 3D MHD numerical simulation code used for heliospheric modeling and space-weather forecasting around the world; e.g., Odstrcil and Pizzo, 2002; Odstrcil *et al.*, 2005; and

references therein), and its potential improvements over other variations in driving ENLIL.

In summary, observations of IPS will play a unique role complementing (and leading) investigations of the inner heliosphere. Space-weather forecasting requires a complex combination of solar, interplanetary, magnetospheric, ionospheric, and geomagnetic observations and measurements. As noted, the strongest geomagnetic storms are produced by the passing of CMEs on the Earth's bow shock. IPS can be used in combination with other remote-sensing techniques to study the "evolution" of CMEs from their onset at the Sun and as they propagate through the inner heliosphere (e.g., Manoharan, 2006; Hardwick *et al.*, 2013; and references therein). Observations of IPS can provide unique information on the shape, size, and velocity of such interplanetary disturbances out to say 3 AU or more distance from the Sun. Therefore, coordinated observations of IPS using the IPS-capable instruments located at different geographic longitudes, in principle, should give the possibility for continuous monitoring of the same plasma features flowing out in the solar wind or one and the same spatial region (A. Gonzalez-Esparza, private communication, 2015). However, there is not currently a unified methodology to infer solar-wind parameters from the observations of IPS and so it is required that the community needs to carry out a survey and testing of the different IPS methodologies in order to unify their results and ensure IPS results are consistent from system to system. This also provides a large potential for continuous CME tracking, for example, as well as much-improved inputs to, say, the UCSD 3D CAT reconstructions, which would allow for higher-resolution results and should further improve the space-weather forecasting capabilities of such a system as well as when using outputs from the UCSD 3D CAT to drive 3D MHD code such as the aforementioned ENLIL or for driving other forms of 3D MHD modeling (e.g., Kim *et al.*, 2014; Jackson *et al.*, 2015b; Yu *et al.*, 2015; and references therein).

13.7 Faraday rotation in heliophysics

An almost-unique means of estimating the true magnetic field of inner-heliospheric structure over wide regions is by Faraday rotation (FR), particularly for large-scale disturbances such as CMEs (Jensen and Russell, 2009; Spangler and Whiting, 2008; Jensen *et al.*, 2010; You *et al.*, 2012). Faraday rotation is the rotation that occurs as an EM wave traverses a birefringent medium such as the plasma of the solar corona and solar wind. It is typically an astrophysical technique that uses pulsars and extragalactic radio sources to study the galactic magnetic field. It is the integrated product of the electron density and the component of the solar magnetic field parallel to the wave vector of the EM wave:

$$FR = \frac{e^3 \lambda^2}{8\pi^2 \epsilon_0 m^2 c^3} \int_{Obs}^{Src} N_e(\mathbf{R})\, \mathbf{B}(\mathbf{R}) \cdot d\mathbf{s} \tag{13.17}$$

for electron density and **B** distributions, $N_e(\mathbf{R})$ and $\mathbf{B}(\mathbf{R})$ (where the parameters are as previously described for the IPS equations earlier in the chapter).

Faraday rotation is the only readily available (and most-obvious) method to measure the magnetic field of the corona on large spatial scales outside of active regions on the solar surface. As a polarized EM wave from a spacecraft, a bright pulsar, the galactic background synchrotron radio emission, a radio galaxy, or other natural radio source propagates through the birefringent plasma of the solar corona or inner heliosphere, the plane of polarization of the EM wave rotates as a function of the magnetic field that is carried by the plasma.

When a CME, propagating outward from the Sun (in an assumed radial motion), crosses the LOS over a period of time, the FR changes due to changes in the electron density and the parallel component of the magnetic field within the CME structure crossing the LOS. The measurements of FR through the corona and inner solar wind have thus far only been carried out at relatively high observing frequencies (~1400 MHz and upwards) and only close-in to the Sun (inside of ~8° elongation/~32 $R_\odot$). The magnitude of FR is proportional to the LOS integral of the plasma density (something which can be obtained through IPS and 3D reconstructions of the inner heliosphere) and the LOS component of the magnetic field.

Determining the intrinsic magnetic field within CMEs (and SIRs/CIRs) as they propagate through the inner heliosphere is thus of utmost importance for the prediction and forecast of incoming events with space-weather potential at the Earth, as already highlighted in the IPS discussion at the end of Sect. 13.3. In all, space-weather prediction is key on the determination of the parameters of velocity, density, and magnetic-field orientation combined, because these are the three main contributing factors determining how geo-effective a CME/SIR/CIR will be.

13.7.1 The potential ionospheric dominance in FR observations

Observations of FR in the inner heliosphere have been carried out before using spacecraft beacons at periods of close conjunction to the Sun (e.g., Jensen and Russell, 2008a, b). However, for a global picture, natural radio sources have to be used – whether they are individual polarized radio sources or the background galactic linearly polarized synchrotron radio emission. In these cases, FR due to both the interstellar medium (ISM) and the Earth's ionosphere need to be taken into account. The magnetospheric contribution is thought to be much smaller and not such a concern. The FR due to the ISM is inherent in the rotation measure (RM)

of an observed pulsar and can be assumed to be constant over the proposed duration of these observations. The ionosphere, however, is much more variable and more of an unknown quantity. Indeed, the variation in the ionospheric FR can be greater than the total contribution of the heliospheric FR itself. Recent results using data from LOFAR (Sotomayor-Beltran *et al.*, 2013) have used total electron content (TEC) maps obtained from Global Positioning Satellite (GPS) data to calculate the expected RM due to the ionosphere and compare this with the measured RM from a number of well-known and well-categorized pulsars. The results are encouraging enough to expect that adequately correcting for the ionosphere is possible via this method and a successful preliminary heliospheric FR observation and slow-solar-wind result has been reported by, e.g., Bisi *et al.* (2014). Using observations from different receiver stations will also result in different RMs with the differences due only to the ionosphere, which could then be used to estimate its overall effect. Any such differences due to the heliosphere should not be noticeable over the range of baselines covered by LOFAR.

13.7.2 Overview of coronal investigations with FR

Previous comparisons have revealed magnetic flux ropes within CMEs where the flux-rope structures measured in situ are often well aligned with the flux cylinder reconstructed in three dimensions using white-light imagery (Jensen *et al.*, 2010). FR observations and **B**-field determination are available from spacecraft transmission signals, non-CME ionospheric backgrounds, and modeling (e.g., Jensen *et al.*, 2010; Sotomayor-Beltran *et al.*, 2013; Jensen *et al.*, 2013a, b; Xiong *et al.*, 2013). Pioneering FR measurements performed by Stelzried *et al.* (1970) using spacecraft-based radio signals not only demonstrated the strong effect of the quiescent solar magnetic field on FR signals, but they also revealed the presence of the magnetic flux ropes (Jensen and Russell, 2008a,b). They also found that a particular advantage of using FR to identify CMEs is that the flux-rope orientation defines its signature in FR with a range of shapes varying from paraboloid dips and hills or via forward and reverse sigmoids. However, this solution was degenerate between the handedness of the helical magnetic field and the orientation of its main axis. The degeneracy could be overcome using a radio telescope capable of simultaneously/near-simultaneously imaging, such as that of LOFAR, or indeed eventually the SKA. Furthermore, Jensen *et al.* (2010) found that the structure varies on the order of hours creating a boundary condition through which to separate out the structure from the background. Results so far established using LOFAR suggest a strong viability of heliospheric FR for both science and as a real potential for future use in space-weather forecasting, but much work is still needed on refining the experiment as well as incorporating other data sources (e.g., You *et al.*, 2012; Sotomayor-Beltran *et al.*, 2013; Bisi *et al.*, 2014).

13.7.3 An introduction to heliospheric FR

A single observation of FR allows the parallel component of the magnetic field to be determined. Therefore, to establish the parallel component in the first instance, the electron density along the LOS needs to be estimated. The column density along the LOS is directly related to the dispersion measure (DM) of the pulsar (i.e., the number of free electrons between us and the pulsar per unit area). The DM (normally determined in units of pc cm^{-3}, where pc is the unit of parsec) is seen as a broadening of the sharp pulse normally observed from the pulsar when the pulse is observed over a finite bandwidth. The density contributions from the ISM are accounted for in the inherent DM of the radio-source signal, leaving only the heliospheric and ionospheric components remaining. The electron density is simply obtained by dividing the DM by the distance to the pulsar (in pc) to provide the electron density, N_e cm^{-3}. Because ionospheric TEC has been demonstrated as being treated sufficiently, leaving only the heliospheric component remaining (e.g., Sotomayor-Beltran *et al.*, 2013), then heliospheric FR is a well-developing scientific and space-weather capability. Ancillary data from coronal and heliospheric white-light imagers and from IPS can also be used to establish general solar-wind conditions along the LOS to model contributions of these conditions to the overall heliospheric DMs and RMs.

For self-consistent modeling of the observed FR, especially when exploiting the continuities along time and space axes, any time-evolving CME model will yield a very-tightly constrained model for the CME flux rope. In fact, using the time series of FR observed along a single LOS provided by satellite beacons, Jensen and Russell (2008a) have successfully constrained the flux-rope orientation, position, size, velocity, rate of change of rope radius and pitch angle. The λ^2 dependence of FR makes the observable effect grow larger with increasing wavelength λ, making it easier to discern at lower frequencies – another reason why LOFAR (and the low-frequency antennas of the SKA) are (will be) perfectly suited receivers for such observations of FR. MWA is another potential radio instrument for observations of FR, and its potential for such is under investigation.

A practical way to observe potential space-weather events will be to initiate FR observations in response to an external trigger, most likely say from a space-based observatory/monitor, which will provide information of the launch time, direction, and transit velocity of a CME. Using this information, and perhaps near-real-time information from IPS or some form of white-light heliospheric imagers, the patch of the sky to be monitored at a given time will be chosen. However, continuous observations from a dedicated system would be preferred both for scientific and forecasting perspectives. It should be noted, though, that the ionospheric FR signal is expected to possibly dominate over the CME FR signal in the bulk of region of interest, and will have its own time and direction dependence. This could be circumvented using multiple simultaneous observations from different receivers.

For a complete unwinding of the FR signal and determination of the southward-component of the magnetic field, multiple observations of FR are necessary. For example, using the background linearly polarized synchrotron radio signal or the polarized signal from multiple individual radio sources as signals pass through a CME's plasma from multiple lines of sight. If a large number of such polarized radio sources are observed along, say, the projected path of a CME on the sky plane, then the results of these FR observations can provide multiple independent values of FR along different lines of sight passing through different parts of the CME. As noted, FR observations are sensitive only to the LOS component of the magnetic field, but like all propagation effects, the observed FR corresponds to the integral along the entire LOS. However, the observations of hundreds (or thousands) of lines of sight through the CME (and the rest of the inner heliosphere) as material travels through the inner heliosphere provide a large number of independent constraints. It is likely that such observations can also be incorporated into tomographic techniques such as those already described for IPS, and these could allow for full three-component magnetic fields to be reconstructed (Jensen *et al.*, 2010; Bisi *et al.*, 2014) as well as for background magnetic fields as can already be achieved with the UCSD CAT (Dunn *et al.*, 2005; Jackson *et al.*, 2015a, b; Yu *et al.*, 2015).

The determination of heliospheric FR, combined with observations of IPS, will have a high potential to provide essential information on the Sun's extended magnetic-field structure out into the inner heliosphere, especially when also combined with other forms of remote-sensing/heliospheric imaging data, and in-situ measurements.